Research Article

Aleksandr Yu. Frolov*, Joris Van de Vondel, Vladimir I. Panov, Pol Van Dorpe, Andrey A. Fedyanin, Victor V. Moshchalkov and Niels Verellen*

Probing higher order optical modes in all-dielectric nanodisk, -square, and -triangle by aperture type scanning near-field optical microscopy

Abstract: All-dielectric nanoantennas, consisting of high refractive index semiconductor material, are drawing a great deal of attention in nanophotonics. Owing to their ability to manipulate efficiently the flow of light within sub-wavelength volumes, they have become the building blocks of a wide range of new photonic metamaterials and devices. The interaction of the antenna with light is largely governed by its size, geometry, and the symmetry of the multitude of optical cavity modes it supports. Already for simple antenna shapes, unraveling the full modal spectrum using conventional far-field techniques is nearly impossible due to the spatial and spectral overlap of the modes and their symmetry mismatch with incident radiation fields. This limitation can be circumvented by using localized excitation of the antenna. Here, we report on the experimental near-field probing of optical higher order cavity modes (CMs) and whispering gallery modes (WGMs) in amorphous silicon nanoantennas with simple, but fundamental, geometrical shapes of decreasing rotational symmetry: a disk, square, and triangle. Tapping into the near-field using an aperture type scanning near-field optical microscope (SNOM) opens a window on a rich variety of optical patterns resulting from the local excitation of antenna modes of different order with even and odd parity. Numerical analysis of the antenna and SNOM probe interaction shows how the near-field patterns reveal the node positions of – and allows us to distinguish between – cavity and whispering gallery modes. As such, this study contributes to a richer and deeper characterization of the structure of light in confined nanosystems, and their impact on the structuring of the light fields they generate.

Keywords: all-dielectric nanophotonics; cavity and whispering gallery modes; higher order modes; nanoantenna; odd and even symmetry; scanning near-field optical microscopy.

*Corresponding authors: **Aleksandr Yu. Frolov**, Faculty of Physics, Lomonosov Moscow State University, Moscow, Russian Federation, E-mail: frolov@nanolab.phys.msu.ru. https://orcid.org/0000-0003-0988-1361; and **Niels Verellen**, imec, Leuven, Belgium; Department of Physics and Astronomy, Quantum Solid-State Physics, KU Leuven, Leuven, Belgium, E-mail: Niels.Verellen@imec.be. https://orcid.org/0000-0001-5110-4158
Joris Van de Vondel and **Victor V. Moshchalkov**, Department of Physics and Astronomy, Quantum Solid-State Physics, KU Leuven, Leuven, Belgium,
E-mail: joris.vandevondel@kuleuven.be (J. Van de Vondel), victor.moshchalkov@kuleuven.be (V.V. Moshchalkov).
Vladimir I. Panov and **Andrey A. Fedyanin**, Faculty of Physics, Lomonosov Moscow State University, Moscow, Russian Federation, E-mail: panov@spmlab.phys.msu.ru (V.I. Panov), fedyanin@nanolab.phys.msu.ru (A.A. Fedyanin). https://orcid.org/0000-0003-4708-6895 (A.A. Fedyanin)
Pol Van Dorpe, imec, Leuven, Belgium; and Department of Physics and Astronomy, Quantum Solid-State Physics, KU Leuven, Leuven, Belgium, E-mail: Pol.VanDorpe@imec.be. https://orcid.org/0000-0003-4708-6895

1 Introduction

All-dielectric nanostructures are becoming key elements in modern nanophotonics R&D, allowing efficient control of the phase, polarization, and direction of light [1]. Two-dimensional arrangements of subwavelength nanoparticles make it possible to create ultrathin metasurfaces [2] operating as efficient lenses [3], polarizers [4], nonlinear [5–9] and magneto-optical devices [10, 11], ultrafast switches [12, 13], light emitting devices [14–16], directional light scatterers [17–20], and photonic topological insulators [21, 22]. A single all-dielectric nanoparticle in such metasurfaces operates as an optical nanoantenna that

manipulates light through the excitation of various electric and magnetic optical modes [23].

The full mode spectrum of a nanoantenna can be significantly expanded by giving it a non-spherical shape. It enables the excitation of higher order modes and thereby offers opportunities for more elaborate light flow manipulation and tunability compared to low order modes. Depending on the spatial field distribution, the higher order modes are localized either inside the whole volume of the nanoantenna – cavity modes (CMs), or around the nanoantenna's edge – whispering gallery modes (WGMs). Spatial and spectral overlapping of higher order CMs and WGMs in nanoantennas complicates their analysis using conventional far-field optical techniques. Moreover, the presence of mirror symmetry planes of complex shaped nanoantennas splits optical modes in ones with even or odd parity (symmetry). As the electromagnetic field of a plane wave source at normal incidence possesses even and odd parity with respect to the two symmetry planes, it allows coupling with only specific modes [24–28]. Whereas modes with mismatching symmetry are forbidden for excitation, inclined illumination is able to break this symmetry coupling rule [29–32]. Numerical works have shown, nevertheless, that a point dipole source can efficiently couple to both even and odd parity modes and as such modify its emission [33–35]. Therefore, local excitation within the near-field becomes a crucial approach to excite and visualize higher order modes in all-dielectric nanoantennas of increasingly complex shapes.

Various optical techniques exist for the local excitation and visualization of optical modes in photonic structures at the nanoscale. The visualization of plasmonic charge density waves in gold microstructures was realized by scanning a plasmonic antenna with a highly focused light beam while recording the scattered intensity [36]. Angular-resolved cathodoluminescence using a high energy electron beam allows the local excitation and mapping of high and low order radial and azimuthal resonant modes in silicon (Si) nanodisks [37], and hybridized symmetric and antisymmetric modes in Si bar dimers [38]. A wide variety of even and odd surface plasmon modes have been mapped using electron beams in metallic nanoantennas of different shapes: rod [39], disk [40], square [41], triangle [42], and their coupled systems [43–45].

Alternatively, the mapping of optical mode distributions with subwavelength resolution can be achieved using scanning near-field optical microscopy (SNOM). Here, either a sharp metal coated needle-like (apertureless) probe or a hollow, metal coated probe with a subwavelength hole at its apex (aperture) is scanned

over the surface of the nanophotonic systems. An SNOM measurement is typically performed with one of two conventional approaches: the collection or illumination scheme.

In the collection scheme, the modes of the nanoantennas are excited from the far-field, and an aperture or apertureless probe picks up their near-field. Such near-field studies have been performed on plasmonic nanoantennas of different shapes including disks, rods, triangles, Yagi-Uda antennas [46–51] and all-dielectric nanoantennas with, e.g., the visualization of electric quadrupole [52] and anapole [53, 54] modes in Si-nanodisks, and the magnetic field in the gap of Si-nanodisk dimers [55]. However, such a technique allows coupling only to a limited number of modes available for plane wave excitation, and tilted illumination should be used in order to access both even and odd parity modes.

In the SNOM illumination scheme, a localized near-field light source is generated around the apex of an aperture or apertureless probe by illuminating it from the far-field. In this case, we obtain a unique subwavelength polarized light source. This localized source can provide a symmetry breaking effect that allows an efficient excitation of even and odd parity modes. As such, multiple plasmonic modes in various antenna shapes [56–59] and optical Fabry–Pérot modes with odd and even parity in amorphous silicon nanorods [60] have been mapped. Notwithstanding that such a variety of higher order optical modes has been observed in plasmonic structures of various shapes, near-field probing of all-dielectric nanoantennas was performed only in disk and rod shapes where several higher order spectrally and spatially separated optical modes have been studied. The modification of a dielectric antenna shape expands the set of higher-order CMs and WGMs with high $Q-$factor. The spectral and spatial overlapping of CMs and WGMs can be exploited to increase the optical density of states which is crucial for light-emitting and non-linear devices. However, the coexistence of multiple spectrally overlapped higher order modes at a single wavelength significantly complicates the analysis and interpretation of SNOM data as compared to a single optical mode.

In the current work, we used the aperture type scanning near-field optical microscopy for the probing of higher CMs and WGMs in all-dielectric nanoantennas with basic geometries of different rotational symmetry. We show experimentally and numerically that the SNOM aperture probe in the illumination scheme excites higher order transverse electric and magnetic modes in disk, square, and triangular antennas consisting of amorphous silicon

(α-Si). Due to the coexistence of a rich variety of modes at a single wavelength, the SNOM maps do not necessarily represent the field distribution of individual optical modes but rather a superposition. Therefore, to provide a thorough analysis of the intensity contrast in SNOM maps, the scanning process of each nanoantenna was simulated with a finite-difference time-domain (FDTD) solver. From these simulations, we can expose the coincidence of features in the SNOM maps and the antennas' electric or magnetic field modal distributions. At the same time, the wavelengths and probe positions that result in resonant excitation of the different modes can be identified by maxima of the electric field localization.

2 Results and discussion

The experimental scheme for the near-field mapping is illustrated in Figure 1(a). The local excitation of the optical modes is obtained by focusing polarized supercontinuum laser light in the wavelength range from $\lambda = 600$ nm to $\lambda = 750$ nm on a subwavelength hole at the apex of 100 nm Al-coated aperture SNOM probe (see the Measurements and simulations in Methods section, Supplementary Materials for more details). The full SNOM map of each nanoantenna is obtained by scanning its surface with the probe in contact mode and recording the transmitted light intensity (T) collected by the objective lens shown at the bottom.

2.1 Disk

We start the discussion with the study of an α-Si nanodisk on a glass substrate. The disk diameter is 515 nm and thickness is 96 nm (see the SEM image in Figure 1(b)). For details on the sample fabrication, we refer to the sample fabrication in Methods section and atomic force microscopy section in Supplementary Materials. Experimental SNOM maps at different wavelengths in the range from $\lambda = 600$ nm to $\lambda = 750$ nm are shown in Figure 1(c). SNOM maps consist of the bright and dark areas corresponding to high and low light transmittance through the SNOM probe–antenna system. The transmittance is modified due to the excitation of higher order optical modes in the nanodisk. The strong wavelength dependence of the patterns in these SNOM maps is similar to the frequency dependence of acoustic Chladni patterns observed on a metallic plate covered by sand and locally driven by a bow [61]. Using full-field 3D FDTD simulations, the experimental maps can accurately be reproduced, as is demonstrated by comparing panel (c) with (d) in Figure 1. The full scanning near-field microscopy configuration is taken into

account for these simulations, including the nanoantenna, the substrate, and the probe (see SNOM simulations in the Methods section, Supplementary Materials for more details). To show how the excited antenna modes modify the probe transmittance T, the color scale is normalized to the transmittance at the glass substrate, T_{sub}, recorded at 3 µm distance from the disk boundary. The nanodisk resonator with high aspect ratio supports a rich variety of coexisting optical modes at the same wavelength. Determining the order and type of the excited modes requires figuring out the probe positions and wavelengths at which resonant excitation occurs. To this end, we calculated the integral of the electric field localized inside the antenna volume, $W_a = \int |E|^2 dV$, recorded at each position of the SNOM probe on the nanoantenna (see SNOM simulations in the Methods section, Supplementary Materials). The spectral dependence of 2D maps of W_a normalized to the electric field localization without antenna W_0 is presented in Figure 1(e). The maxima on these W_a/W_0 maps are located both inside the disk and near its edges. For $\lambda = 610$ nm they are negligible, while for longer wavelengths from $\lambda = 630$ nm to $\lambda = 730$ nm, they are clearly distinguished. The circle, square, diamond, and triangle purple symbols in Figure 1(e) mark the prominent W_a/W_0 maxima located near and far from nanodisk's edge. The near-field distributions of the optical modes shown in the top row of panels (f–i) present FDTD simulations of the dominant field component along z−direction at the wavelengths corresponding to W_a/W_0 maxima. These wavelengths were identified from the spectral dependence of the field localization W_a/W_0 (blue curves in panels (f–i)) recorded at the probe positions marked with the purple symbols on the 2D SNOM (panel (d)) and W_a/W_0 (panel (e)) maps. To categorize the different optical modes supported by the dielectric nanodisk cavity, we follow the nomenclature of microwave dielectric cylindrical resonator antennas and waveguides [63]. TE_{mn}^{ij} designates a hybrid mode which has the $|H_z|$ component as the dominant contribution to the total $|\mathbf{H}|$ field distribution. The subscripts m and n refer to the waveguide mode designation, where m indicates the total number of wavelengths that fit the disk periphery in the azimuthal direction (i.e., half of the antinodes number fitted along the periphery) and n is the number of antinodes fitted along the radial direction. We verify that only one $|H_z|$ antinode exists in the z−direction for the observed modes, i.e., only half of an effective wavelength fits within the antenna thickness. The superscripts $i = e, o$ and $j = e, o$ designate the even (e) or odd (o) mode parity relative to the antenna's mirror symmetry plane perpendicular to the x−axis (σ_x−plane) and y−axis (σ_y−plane),
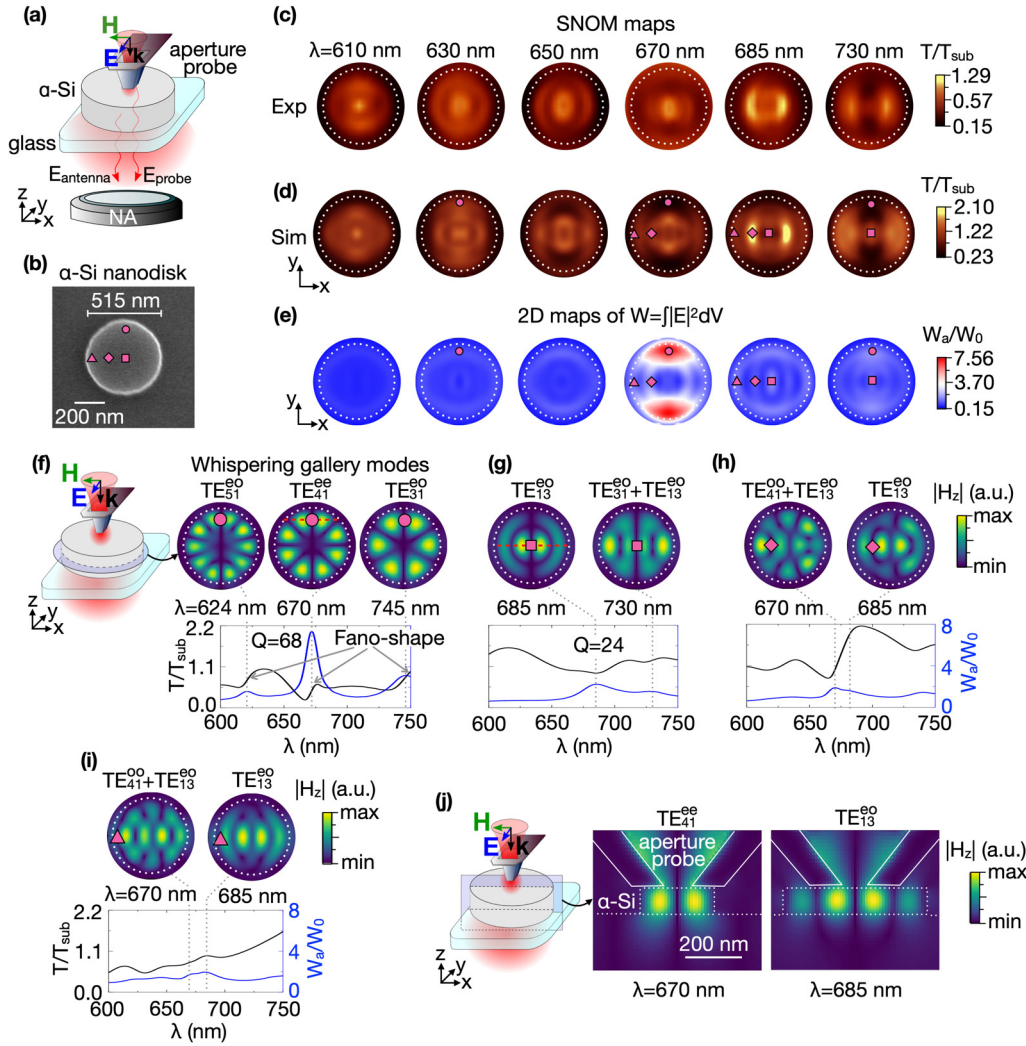
Figure 1: (a) Schematic representation of the near-field mapping of optical modes in the α-Si nanodisk. (b) SEM image of the α-Si nanodisk. The diameter is 515 nm, and the thickness is 96 nm. Experimental (c) and simulated (d) SNOM maps of the α-Si nanodisk at different wavelengths. The polarization of light incident on the SNOM probe (blue arrow) is directed along the $y-$axis. (e) Simulated 2D maps of electric field localization W_a/W_0 at the same wavelengths as in the SNOM maps in (c) and (d). The circle ($x = 0$ nm, $y = 220$ nm), square ($x = 0$ nm, $y = 0$ nm), diamond ($x = 120$ nm, $y = 0$ nm), and triangle ($x = 240$ nm, $y = 0$ nm) symbols on 2D maps in (b), (d), and (e) depict the SNOM probe positions corresponding to maxima of the electric field localization W_a/W_0. (f−i) The simulated SNOM transmittance T/T_{sub} (black curves) and electric field localization W_a/W_0 (blue curves) spectra recorded at the fixed positions of the SNOM probe marked as purple symbols on SNOM (d) and W_a/W_0 (e) maps. The top row in (f−i) shows the simulated $|H_z|$ distributions of TE_{mn}^{ij} optical modes. The $|H_z|$ field was taken at central $xy-$cross-sections of the nanodisk as shown in the sketch in panel (f). (j) $|H_z|$ distributions of TE_{41}^{ee} and TE_{13}^{eo} optical modes at $xz-$cross-section (see schematic illustration in the sketch). The positions of $xz-$plane cuts are marked by red dashed lines in (f) and (g). Dotted white circles indicate the boundary of the nanodisk. The solid white lines indicate the edges of the aperture SNOM probe.

respectively. Since the magnetic field **H** is a pseudovector, the H_z component of even parity modes transforms as an antisymmetric function ($H_z(x, y) = -H_z(-x, y), H_z(x, y) = -H_z(x, -y)$) under mirror reflections with respect to σ_x and σ_y planes, and as a symmetric function ($H_z(x, y) = H_z(-x, y), H_z(x, y) = H_z(x, -y)$) in the case of odd parity modes.

When the probe locates near the edge of the disk (circle symbol marking in Figure 1(f)), the W_a/W_0 spectrum has

three maxima which correspond to the excitation of the following WGMs: TE_{51}^{eo} at $\lambda = 624$ nm, TE_{41}^{ee} at $\lambda = 670$ nm, and TE_{31}^{eo} at $\lambda = 745$ nm. It is also observed that the SNOM probe positions, that result in resonant excitation, coincide with the $|H_z|$ nodes of these WGMs.

Next, we discuss the optical modes excited at other probe positions. When the probe locates in the disk center (square mark in Figure 1(g)), the type of modes changes from WGMs, which are mostly concentrated near the disk

edge, to CMs, which cover the full disk volume. The maximum at $\lambda = 685$ nm of the corresponding W_a/W_0 spectrum is associated with the TE_{13}^{eo} mode (σ_x−even, σ_y−odd). Due to the arrangement of three $|H_z|$ antinodes along the x−axis (counting from the center of the disk), the TE_{13}^{eo} mode is again excited by the SNOM probe at the two off-center positions marked as diamond and triangle in Figure 1(h) and (i), respectively. These positions also coincide with $|H_z|$ nodes of the TE_{13}^{eo} mode. In addition to the excitation of individual modes, Figure 1(g) shows that the probe simultaneously excites a superposition of modes at the square mark position at $\lambda = 730$ nm (superposition of TE_{31}^{eo} and TE_{13}^{eo} modes). The superposition of TE_{41}^{oo} and TE_{13}^{eo} modes is observed at the positions marked as diamond (panel (h)) and triangle (panel (i)) at $\lambda = 670$ nm. This simultaneous excitation occurs when the individual modal antinodes and spectral bands overlap (see Section 3, Supplementary Materials with the decomposition of the H_z field distribution in the individual eigenmodes).

The positions of the SNOM probe, at which the resonant excitation takes place, coincide with nodes of the $|H_z|$ distribution for all excited optical modes. Figure 1(j) shows in more detail the coupling of the probe near-field with TE_{41}^{ee} and TE_{13}^{eo} modes. It presents the simulated $|H_z|$ field distribution in the xz−plane (see sketch in (j)) taken through the circle and square probe positions along the red dashed lines in (f) and (g). The SNOM probe near-field, created by the incident focused laser light with linear polarization, possesses two strong $|H_z|$ hotspots (see also field distribution of all components near the aperture SNOM probe in Supporting Information in Ref. 56). At the position of the modal $|H_z|$ nodes, the two magnetic field hotspots of the probe apex spatially overlap with two $|H_z|$ antinodes of TE_{41}^{ee} and TE_{13}^{eo} modes resulting in the resonant excitation. The reason for the efficient excitation of optical modes at the node of the normal field components is the absence of the normal magnetic field component at the center of the SNOM probe [56, 62]. In contrast to the zero normal magnetic component, a strong lateral electric field component (along the y-axis) exists at the center of the SNOM probe. Therefore, the resonant position also corresponds to the antinodes of the lateral electric field. Similar correspondence of lateral field antinodes with resonant position of the SNOM probe has been observed for plasmonic [56, 58] and all-dielectric nanoantennas [60].

Now we discuss the transmission intensity contrast that is observed in the SNOM maps. For this, we focus on the most prominent W_a/W_0 maxima positions in Figure 1(e) and superimpose them on the simulated SNOM maps in Figure 1(d) (purple marks). As such, we can associate the excitation of specific optical modes with the resulting transmittance features. A quick look at Figure 1(d) and (e) already reveals that there is no straightforward one-to-one correlation between the excitation of a mode and the SNOM contrast. Indeed, the maxima of the field localization can coincide with both local dark or bright spots, or even somewhere in between. This leads us to conclude that the SNOM intensity contrast is the result of a more intricate interplay between multiple coexisting optical modes that can be excited at the same wavelength. The scattering intensity of each optical mode can be high or low, which results in bright or dark spots, respectively. For the SNOM map at $\lambda = 630$ nm (Figure 1(d)), TE_{51}^{eo} WGM excitation results in the bright spot. The other T/T_{sub} maxima and minima on this SNOM map near the disk center are also associated with the excitation of other higher order modes. However, their electric field localization is lower than that of TE_{51}^{eo}. For the SNOM map at $\lambda = 685$ nm, TE_{41}^{ee} WGM excitation leads to the dark spot (circle in Figure 1(d)), while the $TE_{41}^{oo} + TE_{13}^{eo}$ mode appears as local bright spots at the diamond and triangle dots. For the SNOM map at $\lambda = 685$ nm, the excitation of the TE_{13}^{eo} mode at their three $|H_z|$ nodes (square, diamond, and triangle) results in three bright spots with various T/T_{sub} values of 0.9, 2.1, 0.97, respectively. Finally, for the SNOM map at $\lambda = 730$ nm, the TE_{31}^{eo} WGM appears as the local dark spot (circle mark), but the $TE_{13}^{eo} + TE_{31}^{eo}$ mode leads to the bright spot (square mark).

Figure 1(g)−(i) depicts the spectral dependence of the transmittance T/T_{sub} (black curves) and field localization W_a/W_0 (blue curves), for fixed positions of the SNOM probe as indicated with the purple dots in Figure 1(d) and (e). Also here, it is seen that there is no straightforward link between the local excitation of a mode and the resulting T/T_{sub} behavior, i.e., there is no spectral match between peaks and dips. A closer look, however, reveals that the T/T_{sub} curves possess asymmetric Fano lineshapes in the spectral vicinity of resonant modes excitation (the W_a/W_0 maxima). The asymmetric lineshape arises from the interference of the two radiative contributions reaching the objective: the first one being the resonant radiation of an optical mode ($E_{antenna}$, see Figure 1(a)) and the second being light non-resonantly transmitted through the antenna (E_{probe}, see Figure 1(a)). The latter comes from propagating modes of the illuminated probe [64]. Similar spectral behavior of the transmittance spectrum (Fano lineshape) has been observed for plasmonic nanoantennas probed by aperture type SNOM in the illumination mode [65, 66]. The T/T_{sub} minima (maxima), which are

blue-(red-) shifted from the W_a/W_0 maxima in Figure 1(f–i), are the results of the destructive (constructive) interference between the antenna modes and propagating modes of the probe. Consequently, this Fano-interference, along with various scattering intensities of each mode, influences the SNOM map intensity contrast. Each mode can manifest itself as a bright or dark spot depending on the observation wavelength and the transmittance of other coexisting modes. Moreover, the SNOM probe position determines the transmittance properties of the individually excited mode. It is seen from the excitation of the TE_{13}^{eo} mode at its three $|H_z|$ nodes (square, diamond, and triangle symbols in panel (d) at $\lambda = 685$ nm) where three bright spots correspond to different T/T_{sub} values of 0.9, 2.1, and 0.97, respectively. The corresponding electric field localization values are 2.27, 1.49, 1.92, and correlate oppositely with the T/T_{sub} values. W_a/W_0 at the second $|H_z|$ node (diamond, Figure 1(h)) is lower than at two other nodes (square and triangle in Figure 1(g) and (i), respectively). The lower W_a/W_0 at the second $|H_z|$ node means lower coupling efficiency of the probe near-field with the TE_{13}^{eo} mode resulting in higher non-resonant scattering intensity from the SNOM probe and therefore a brighter spot on the SNOM maps. The coupling efficiency at the second $|H_z|$ node (diamond mark) is lower as the SNOM probe near-field is coupled with two $|H_z|$ antinodes of different spatial shapes (one circular and one half-moon shaped) in comparison with ones at the center and edge positions (see $|H_z|$ distribution of TE_{13}^{eo} mode in panels (g, h, i)). Hence, the T/T_{sub} contrast of an individual excited optical mode is also modified when the probe drives the same mode at its different $|H_z|$ nodes. An additional contribution to the modification of the T/T_{sub} value, appearing when the same mode is excited at its different nodes, is the dependence of the phase shift between resonant and non-resonant radiation on the relative position of the SNOM probe and the nanoantenna's center. The phase shift is modified when the probe excites the same mode at its nodes which are closer or further from the antenna's center.

Compared with other works on SNOM near-field mapping, the observed SNOM contrast for the α-Si nanodisk is different from the contrast observed for the excitation of the spectrally and spatially separated Fabry–Perot modes in all-dielectric [60] and plasmonic 1D nanorod [56, 67] antennas. In those nanoantennas, the bright (for dielectric nanorod) and dark (for plasmonic nanorod) spots on the SNOM maps coincide with the probe positions of resonant excitation. However, similar to the obtained SNOM maps for a α-Si nanodisk, the coexisting cavity and edge plasmon modes at a single wavelength results in either bright or dark spots on SNOM maps measured on gold nanodisks [68] and graphene nanoresonators with a disk and square shape [69].

To conclude, for the disk antenna geometry, we showed that near-field light of the SNOM aperture probe locally excites the higher order TE_{mn}^{ij} CMs and WGMs in the α-Si nanodisk. Within our experimental spectral range, we observed modes with indices $m = 1$–5 and $n = 1$–3. The parity (i, j) of the excited modes can be either even or odd for two orthogonal symmetry mirror planes of the disk. The visualized TE_{mn} modes are different from the higher order TM_{mn} modes (E_z component is dominant, and $m = 0$–4, $n = 1$–4) that were observed by electron beam excitation of a Si-nanodisk [37] and an apertureless SNOM approach [52]. In our study, the simulations of near-field distributions show that the positions where the probe excites optical modes, coincide with $|H_z|$ nodes of the TE_{mn}^{ij} modes. The SNOM maps do not directly represent the field distribution of individual optical modes, but rather a superposition due to the coexistence of a rich variety of modes. The excitation of disk modes results in either bright (high scattering) or dark (low scattering) spots on SNOM maps. The varying intensity contrast seen in the SNOM maps is associated with the scattering intensity of each excited mode, Fano-interference between the mode and probe radiation, and varying coupling efficiency of the probe's near-field with the optical modes at their different nodes.

2.2 Square

Next, we reduce the antenna rotational symmetry to four-fold and turn our attention to an α-Si nanosquare with dimensions similar to the nanodisk above: side length of 515 nm and thickness of 96 nm (see SEM image in Figure 2(a)). The experimental and simulated SNOM maps are shown in Figure 2(b) and (c), respectively, at multiple wavelengths between $\lambda = 600$ nm and $\lambda = 750$ nm. Also here, very distinct transmission patterns are obtained with a very good agreement between experiment and simulation. Although these patterns present some resemblance to those of the nanodisk, there are some clear differences. The calculated 2D maps of electric field localization W_a/W_0 shown in Figure 2(d) reveal the probe positions of resonant mode excitation at the local W_a/W_0 maxima. The prominent W_a/W_0 maxima positions – near and far from the square's edges – are again marked in Figure 2(a) and (d) with a purple symbol. To find the exact wavelengths of resonant mode excitation, W_a/W_0 (blue curves) spectra taken at fixed probe positions are shown in Figure 2(e–h). The top row depicts the distribution of the dominant field component $|H_z|$ in the nanosquare taken at
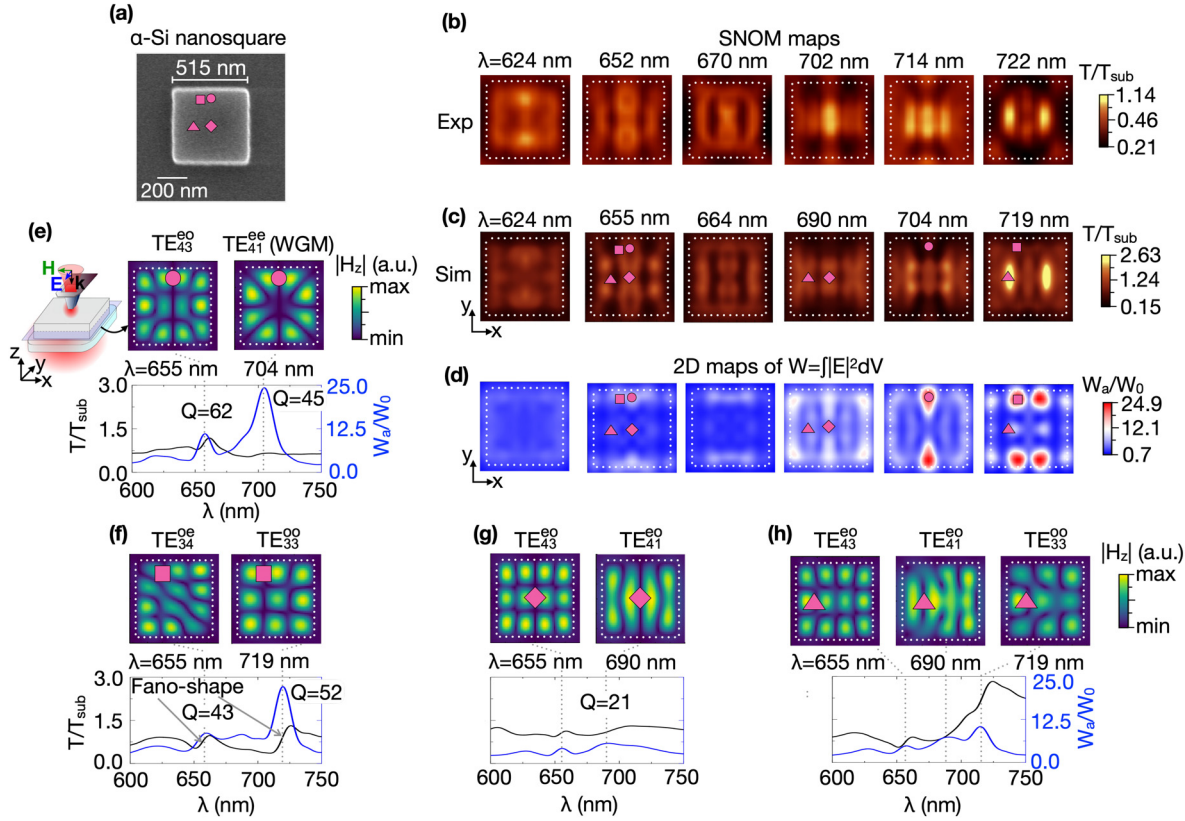
Figure 2: (a) SEM image of the α-Si nanosquare. The side length is 515 nm, and the thickness is 96 nm. Experimental (b) and simulated (c) SNOM maps of the α-Si nanosquare at different wavelengths. The polarization of the light incident on the SNOM probe (blue arrow) is directed along the $y-$axis. (d) Simulated 2D maps of electric field localization W_a/W_0 at the same wavelengths of the SNOM maps in (c). The circle ($x = 0$ nm, $y = 220$ nm), square ($x = 80$ nm, $y = 200$ nm), diamond ($x = 0$ nm, $y = 0$ nm), and triangle ($x = 120$ nm, $y = 0$ nm) symbols on 2D maps in (a), (c), and (d) depict the SNOM probe positions corresponding to maxima of electric field localization. (e–h) The simulated SNOM transmittance T/T_{sub} (black curves) and electric field localization W_a/W_0 (blue curves) spectra recorded at the fixed positions of the SNOM probe marked as purple symbols on SNOM (c) and W_a/W_0 (d) maps. The top rows in (e–h) show the simulated $|H_z|$ distributions of TE_{mn}^{ij} optical modes. The $|H_z|$ field was taken at central $xy-$cross-sections of the nanosquare as shown in the sketch in panel (e). Dotted white lines indicate the boundary of the nanosquare.

wavelengths corresponding to W_a/W_0 maxima in the plots at the bottom row. The $|H_z|$ distributions reveal that the probe excites TE_{mn}^{ij} optical modes, which have $|H_z|$ as the dominant contribution to the total $|\mathbf{H}|$ field. The subscripts m and n in TE_{mn}^{ij} indicate the number of $|H_z|$ antinodes in x, $y-$direction, respectively. There is only one antinode in the $z-$direction for the observed modes. Two W_a/W_0 maxima at $\lambda = 655$ nm and $\lambda = 704$ nm in panel (e) are associated with the excitation of TE_{43}^{eo} CM and TE_{41}^{ee} WGM (subscripts for TE_{41}^{ee} mode correspond to the designation of a WGM in a disk) when the probe locates at the position near the square's edge marked with the circle. At the square mark position, shown in panel (c) at $\lambda = 655$ nm, the SNOM probe excites the TE_{43}^{eo} mode. The SNOM probe also launches the same TE_{43}^{eo} mode at two other positions. The first is at the center of the nanosquare (panel (g), diamond, $\lambda = 655$ nm). The second is near the left edge (panel (h),

triangle, $\lambda = 655$ nm). In addition to the excitation of the TE_{43}^{eo} mode with even parity with respect to the σ_x-plane and odd parity with respect to the σ_y-plane, panel (f) shows the excitation of TE_{34}^{oe} at the off-center probe position marked with the square ($\lambda = 655$ nm) having the opposite symmetry to TE_{43}^{eo}. Along with TE_{34}^{oe}, the probe excites TE_{33}^{oo} at the square mark position and $\lambda = 719$ nm (Figure 2(f)). This mode is again launched at the triangle mark position at $\lambda = 719$ nm (panel (h)), but with smaller efficiency, since this position does not precisely correspond to the maximum of W_a/W_0 (see 2D W_a/W_0 map in panel (d)). The last CM observed is TE_{41}^{eo} which is excited at $\lambda = 690$ nm at the diamond (panel (g)) and triangle (panel (h)) mark. As it was for the disk case, probe positions corresponding to resonant excitation coincide with $|H_z|$ nodes of these TE_{mn}^{ij} modes.

Similar to the SNOM maps of the nanodisk, superimposing the W_a/W_0 maxima in Figure 2(d) onto the SNOM maps in Figure 2(c) highlights the transmittance features associated with the excitation of the optical modes. The excitation of multiple coexisting modes at their various $|H_z|$ nodes results in bright and dark spots on the SNOM maps. In panel (c), e.g., the bright and dark areas at $\lambda = 655$ nm are associated with the excitation of TE_{43}^{eo} and TE_{34}^{oe} CMs. TE_{43}^{eo} excited at its central $|H_z|$ node (square mark) results in the local dark spot on the SNOM map, while excitation of TE_{43}^{eo} at its off-center nodes results in a transmission intensity somewhere between the bright and dark spots (circle and triangle). Similar to the disk case, the excitation of TE_{43}^{eo} CM at either its center or off-center $|H_z|$ node positions, gives rise to a different T/T_{sub} value, an effect that can be ascribed to a position dependent coupling efficiency between probe and mode. However, compared to the disk case, the T/T_{sub} maxima/minima show a larger spatial shift relative to the W_a/W_0 maxima as a result from the excitation of the square's TE_{43}^{eo} mode at its off-center nodes (circle and triangle). The intermediate T/T_{sub} values observed at W_a/W_0 maxima positions can intuitively be explained by the probe position dependence of the phase shift between the optical mode radiation and non-resonant probe radiation. When the probe is closer to/farther from the antenna center, the phase shift decreases/increases since the excited mode does not change its spatial position with respect to the antenna center during the scanning process. It results in the decrease/increase of the transmitted light (dark/bright areas) near the $|H_z|$ node positions. Suppose one of the two channels (antenna mode or non-resonant probe radiation) is negligible. In that case, the phase shift change does not lead to a significant spatial shift of the T/T_{sub} minima/maxima with respect to the W_a/W_0 maxima (as it was observed for the disk case). Following this, the phase change effect is more pronounced for TE_{43}^{eo} modes than for the previously discussed TE_{mn}^{ij} modes in the nanodisk due to the (approximately) equal contribution of the resonant and non-resonant radiation. Similar behavior is observed on the SNOM map at $\lambda = 690$ nm for the excitation of the TE_{41}^{eo} mode at its various $|H_z|$ nodes. The local bright spot appears on the SNOM map at $\lambda = 690$ nm at the central $|H_z|$ node position of TE_{41}^{eo} (diamond, panel (c)). However, the off-center node of this mode (triangle, panel (c)) is between the bright and dark areas. For the SNOM map at $\lambda = 704$ nm, the node of TE_{41}^{ee} WGM is also between the bright and dark areas (panel (c), circle). For the SNOM map at $\lambda = 719$ nm, TE_{33}^{oo} mode excitation results in two local bright spots with different relative T/T_{sub} at the square and triangle mark.

The different T/T_{sub} values, associated with excitation of optical modes, are also demonstrated in Figure 2(e–h) by the simulations of the T/T_{sub} (black curves) and W_a/W_0 (blue curves) spectral dependences recorded at individual SNOM probe positions marked with the purple dots. Similar to the disk case, T/T_{sub} curves present asymmetric Fano lineshapes near the vicinity of optical mode excitation (W_a/W_0 maxima) caused by interference of the antenna mode radiation and non-resonantly transmitted light. This again shows that the different modes result in various T/T_{sub} Fano lineshapes. Even for the individual modes, TE_{43}^{eo} and TE_{33}^{oo}, excited at their different $|H_z|$ nodes, the T/T_{sub} values and Fano lineshapes differ. The different Fano lineshapes are also associated with changes in a phase shift and coupling efficiency when modes are excited at their different $|H_z|$ nodes.

To summarize for the square geometry, SNOM maps of the α-Si nanosquare reveal the excitation of higher order TE_{mn}^{ij} WGM $((m,n) = (4,1))$ and CMs $((m,n) = (4,1); (3,3); (3,4); (4,3))$ with either even or odd parity (i,j). The observed chess-like $|H_z|$ field distribution of TE_{mn}^{ij} CMs in the square antenna differs from the disk case due to the difference in the light reflection conditions at the two opposite parallel edges of the square compared to the rounded edges in the disk antenna cavity. Similar to the disk case, the intensity contrast of each SNOM map at a single wavelength results from the superposition of spectrally overlapping higher order TE_{mn}^{ij} CMs and WGMs. The SNOM probe positions of the resonant excitation occurring at $|H_z|$ nodes of TE_{mn}^{ij} modes, coincide with local bright and dark areas on the SNOM maps as was for the disk case, but now also at intermediate transmission values. The SNOM contrast is again associated with various scattering intensities of the excited modes, the Fano-interference between the probe and mode radiation, and the different coupling efficiency of the probe near-field to the modes.

2.3 Triangle

Reducing the rotational symmetry of the nanoantenna further expands the modal spectra. In contrast to the disk and square shape, for the equilateral triangle possessing mirror symmetry only with respect to the σ_x–plane, a 90° change in the excitation polarization allows the SNOM probe to couple to a different set of modes [70]. Therefore, the polarization directions parallel and perpendicular with respect to the triangle's height (y–axis) are studied separately in Figures 3 and 4, respectively. Starting with parallel polarization in Figure 3, the experimental SNOM maps of an equilateral α-Si nanotriangle with a side length of 700 nm
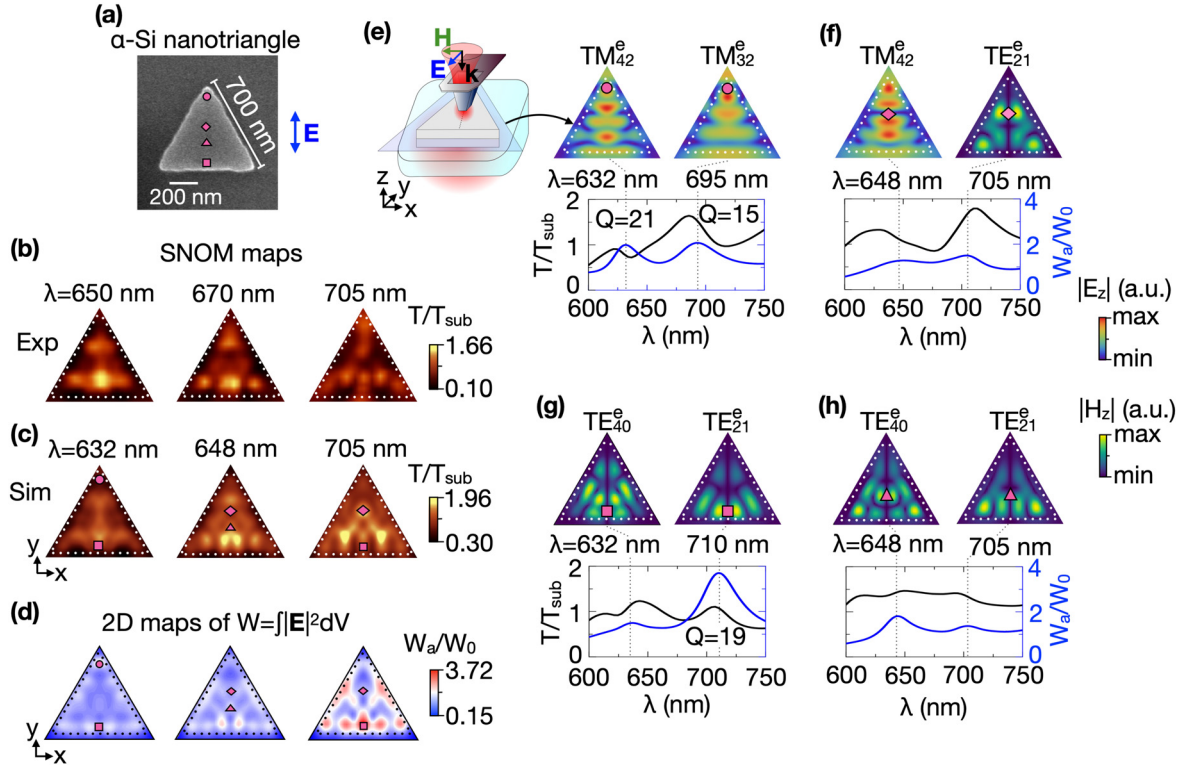
Figure 3: (a) SEM image of the equilateral α-Si nanotriangle. The side length of triangle is 700 nm, and the thickness is 100 nm. The blue arrow indicates the $y-$polarization of light focused in the SNOM probe. Experimental (b) and simulated (c) SNOM maps of the α-Si equilaterale nanotriangle for $y-$polarized excitation. (d) Simulated 2D maps of electric field localization W_a/W_0 at the same wavelengths of the SNOM maps in (c). The circle ($x = 0$ nm, $y = 580$ nm), square ($x = 0$ nm, $y = 120$ nm), diamond ($x = 0$ nm, $y = 360$ nm), and triangle ($x = 0$ nm, $y = 260$ nm) symbols on (a), (c), and (d) depict the SNOM probe positions corresponding to maxima of electric field localization. (e−h) The simulated SNOM transmittance T/T_{sub} (black curves) and electric field localization W_a/W_0 (blue curves) spectra recorded at the fixed positions of the SNOM probe marked as purple symbols on the SNOM (c) and W_a/W_0 (d) maps. The top rows in (e−h) show the simulated $|E_z|$ and $|H_z|$ distributions for TM_{mn}^e and TE_{mn}^e modes, respectively. The $|E_z|$ and $|H_z|$ field was taken at central $xy-$cross-sections of the nanotriangle as shown in the sketch in panel (e). Dotted white and black lines indicate the boundary of the nanotriangle.

and thickness of 100 nm (see SEM image in panel (a)) are shown in panel (b) together with the simulated results in panel (c). Again, the simulated SNOM maps demonstrate a good agreement with the experimental results. Maxima on the 2D W_a/W_0 maps in Figure 3(d) marked with the purple symbols indicate probe positions that result in resonant mode excitation. For the triangle antenna, we limit our discussion to probe positions on the triangle's height from the top corner to the base.

The field distribution in Figure 3(e−h) taken at the fixed probe positions (marked by purple symbols in panel (d)) and corresponding to maxima of W_a/W_0 spectra (blue curves) in Figure 3(e−h) demonstrate the excitation of both TM_{mn}^i and TE_{mn}^i modes with dominant $|E_z|$ and $|H_z|$ components, respectively. The TM_{mn}^i as well as the TE_{mn}^i modes can be excited by the SNOM probe due to the existence of two intense $|E_z|$ hotspots near the SNOM probe aperture along the $y-$direction. These two $|E_z|$ hotspots resonantly

couples with two $|E_z|$ antinodes of TM_{mn}^i modes at their $|E_z|$ node positions. More details on the distributions of all field components near the aperture SNOM probe can be found in the Supporting Information of Ref. 56. The indices m and n refer to analytical solutions for TM and TE waveguide modes with even and odd parity (with respect to the σ_x-plane perpendicular to the $x-$axis) for a hollow equilateral triangle waveguide with metal walls [71, 72]. These modes have a similar spatial arrangement of antinodes as the dielectric triangle cavity [70, 73] (see analytical solutions in Section 4, Supplementary Materials). The E_z component is transformed under mirror reflection with respect to the σ_x-plane with symmetric function ($E_z(-x, y) = E_z(x, y)$) for even symmetry modes, while the H_z component is transformed as an antisymmetric function ($H_z(x, y) = -H_z(-x, y)$) since **H** is a pseudovector. When the probe locates near the top corner (panel (e), circle), TM_{42}^e and TM_{32}^e modes with the dominant $|E_z|$ component
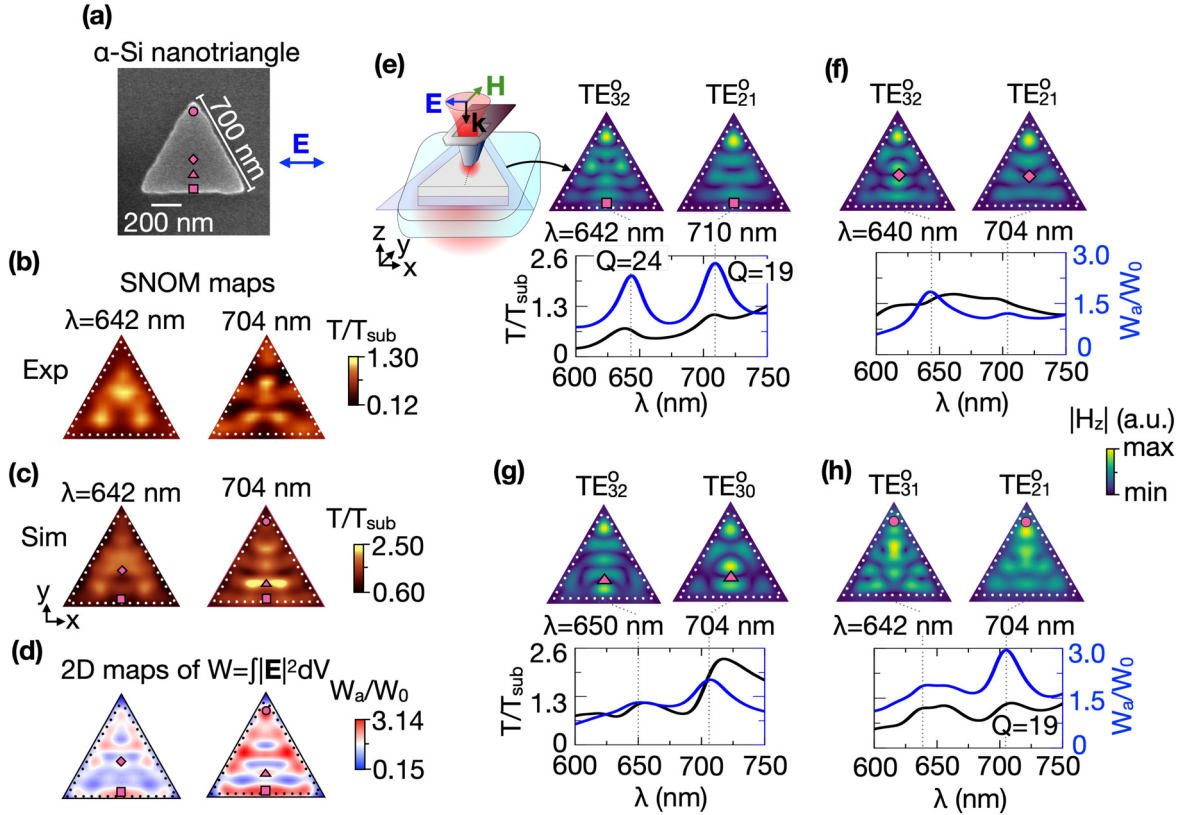
Figure 4: (a) SEM image of the equilateral α-Si nanotriangle (the same as in Figure 3). The side length of triangle is 700 nm, and the thickness is 100 nm. The blue arrow indicates the x−polarization of light focused in the SNOM probe. Experimental (b) and simulated (c) SNOM maps of the α-Si equilaterale nanotriangle for x−polarized excitation, respectively. The blue arrow indicates the x−polarization of light focused in the SNOM probe. (d) Simulated 2D maps of electric field localization W_a/W_0 at the same wavelengths of the SNOM maps in (c). The circle ($x = 0$ nm, $y = 560$ nm), square ($x = 0$ nm, $y = 80$ nm), diamond ($x = 0$ nm, $y = 260$ nm), and triangle ($x = 0$ nm, $y = 180$ nm) symbols on (a), (c), and (d) depict the SNOM probe positions corresponding to maxima of electric field localization. (e–h) The simulated SNOM transmittance T/T_{sub} (black curves) and electric field localization W_a/W_0 (blue curves) spectra recorded at the fixed positions of the SNOM probe marked as purple symbols on SNOM (c) and W_a/W_0 (d) maps. The top rows in (e–h) show the simulated $|H_z|$ distributions of TE^o_{mn} modes. The $|H_z|$ field was taken at central xy−cross-sections of the nanotriangle as shown in the sketch in panel (e). Dotted white and black lines indicate the boundary of the nanotriangle.

are excited at $\lambda = 632$ nm and $\lambda = 695$ nm, respectively, having even symmetry with respect to the σ_x−plane. TM^e_{42} is also excited at the position marked with the diamond in Figure 3(f) at $\lambda = 648$ nm. At this position, the probe also excites TE^e_{21} at $\lambda = 705$ nm (Figure 3(f)). Figure 3(g) shows excitation of TE^e_{40} ($\lambda = 632$ nm) and TE^e_{21} $\lambda = 710$ nm) when the probe locates near the bottom side of the triangle (position marked with the square). Figure 3(h) demonstrates that TE^e_{40} ($\lambda = 632$ nm) and TE^e_{21} ($\lambda = 705$ nm) modes are excited again at the position marked with the triangle.

The positions of resonant excitation coincide with $|E_z|$ nodes for TM^e_{mn} and $|H_z|$ nodes for TE^e_{mn}. These positions, superimposed on the SNOM maps (purple symbols in Figure 3(c)), show that coexisting optical modes result in various T/T_{sub} contrast on an SNOM map due to their different scattering intensities and Fano-interference

between the non-resonant probe and antenna radiation. For the SNOM map at $\lambda = 632$ nm (Figure 3(c)), the local dark spot near the triangle's corner (see circle at $\lambda = 632$ nm in Figure 3(c)) results from TM^e_{42} excitation. While the square mark position near the triangle's bottom (panel (c)), corresponding to TE^e_{40} excitation, is located between a bright and dark area. For the SNOM map at $\lambda = 648$ nm, the local bright spot at the triangle mark position and the dark one at the diamond mark position appear due to the TE^e_{40} and TM^e_{42} modes excitation, respectively. Finally, for the SNOM map at $\lambda = 705$ nm, the first $|H_z|$ node of TE^e_{21} coincides with the local bright spot at the diamond mark, while the second one locates between bright and dark areas (square). Such difference of T/T_{sub} value for the TE^e_{21} mode is again associated with the different coupling efficiency of the probe near-field with the

TE_{21}^{e} mode at two different $|H_z|$ node positions. The second reason is a different phase shift between the resonant and non-resonant radiation for the two different probe positions.

Figures 4(b) and (c) show that rotation of the excitation polarization by 90° leads to modification of the SNOM maps due to the absence of mirror symmetry of the nanotriangle with respect to the σ_y-plane (perpendicular to the $y-$axis). Again, experimental maps (panel (b)) are in very good agreement with simulated results (panel (c)). The selected wavelengths of $\lambda = 642$ nm and $\lambda = 704$ nm correspond to the maxima on the W_a/W_0 maps shown in panel (d). The simulated $|H_z|$ distributions shown in panels (e−h) demonstrate that the type of modes excited along the height of the triangle is transverse electric with odd parity with respect to the σ_x-plane. The mode parity is opposite to the one observed for $y-$polarized illumination (Figure 3). The H_z field distribution of the modes for $x-$polarized illumination is transformed as a symmetric function ($H_z(x, y) = H_z(-x, y)$). The TE_{32}^{o} ($\lambda = 642$ nm) and TE_{21}^{o} ($\lambda = 710$ nm) modes (panel (e)) are excited at the position marked with the square near the bottom side of the triangle. TE_{32}^{o} and TE_{21}^{o} are also excited when the probe locates near the center of the nanotriangle (diamond in panel (f)). TE_{21}^{o} is also excited near the corner of the nanotriangle (panel (h), circle at $\lambda = 704$ nm). Panel (g) shows the distribution of a TE_{30}^{o} mode at $\lambda = 704$ nm which is excited at the triangle mark probe position. One more mode is TE_{31}^{o} which is excited near the top corner (circle in panel (h) at $\lambda = 642$ nm).

The superimposed W_a/W_0 maxima positions on the simulated SNOM maps (Figure 4(c)) show the various SNOM probe transmittance features associated with the excitation of coexisting optical modes with different scattering intensity, similar to the disk and square case. For the SNOM map at $\lambda = 642$ nm, TE_{32}^{o} excitation results in the local dark spot at the triangle's bottom (square mark) and the bright spot at the diamond mark position. At $\lambda = 704$ nm, the local bright and dark spot near the triangle's bottom (square mark) and corner (circle mark), respectively, result from TE_{21}^{o} mode excitation. Another local bright spot at the triangular mark position corresponds to TE_{30}^{o} mode excitation. As is the case for the disk and square geometry, Fano resonance lineshapes in the transmission spectra, recorded at fixed probe positions, are also observed for the nanotriangle's TE_{nm}^{i} and TM_{nm}^{i} modes, and this for both excitation polarizations (see T/T_{sub} spectra in panels (e−h) in Figures 3 and 4).

Concluding the triangle geometry, the bright and dark spots on the observed SNOM maps are associated with excitation of TE_{mn}^{i} ($(m, n) = (4, 0), (3, 2), (3, 1), (3, 0), (2, 1)$) and TM_{mn}^{i} ($(m, n) = (4, 2), (3, 2)$) higher order optical modes. The dark and bright features are linked with TE_{mn}^{i} or TM_{mn}^{i} modes by simulations of the electric field localization and field distributions. Similar to the disk and square antennas, the bright and dark features on the SNOM maps appear due to the differences in scattering intensities of the excited modes, the Fano-interference between the probe and mode radiation, and difference in coupling efficiency of the probe near-field with the modes. In addition, the change of the illumination polarization leads to a modification of the mode parity of the excited optical modes. The positions of resonant excitation coincide with $|E_z|$ nodes for TM_{mn}^{e}, and $|H_z|$ nodes for TE_{mn}^{e} and TE_{mn}^{o}.

2.4 Quality factor and light trapping capabilities of the excited modes

In addition to the far-field radiative properties of the locally excited higher order modes, we estimate their $Q-$factors and light trapping capabilities, which are important parameters for applications in light-emitting devices, solar cells, and non-linear light generation. For this, the W_a/W_0 spectra of the nanodisk (Figure 1(f) and (g)), nanosquare (Figure 2(e)−(g)), and nanotriangle (Figure 3 (e and g) and Figure 4(e and h)) were fitted with a multipeak Lorentzian. For the nanodisk, the highest quality factor of $Q = 68$ and highest field localization value of $W_a/W_0 = 7.5$ are obtained for TE_{41}^{ee} WGM. These values are higher in comparison with other higher order CMs of the nanodisk ($Q = 24$ and $W_a/W_0 = 2.3$ for TE_{13}^{eo}) and the lowest order modes in a Si nanodisk (magnetic or electric dipole modes [74]).

A slightly lower $Q = 45$ is observed for TE_{41}^{ee} WGM (Figure 2(e)) in the nanosquare. This can be attributed to the additional scattering experienced by the WGM at the sharp corners of the square. The cavity modes in the nanosquare, on the other hand, have $Q = 63$ and $Q = 52$ for TE_{43}^{eo} (Figure 2(e)) and TE_{33}^{oo} (Figure 2(f)), respectively. This is higher in comparison to the CMs in the nanodisk and comparable with its TE_{41}^{ee} WGM. A higher $Q-$factor for the CMs in the nanosquare can be explained by its well-defined cavity length defined by the two opposite parallel edges, which are absent in a disk and triangle. A lower $Q-$factor of 21 is observed for the TE_{41}^{eo} CM in the nanosquare. Interestingly, for the TE_{33}^{oo} CM and TE_{41}^{ee} WGM in the nanosquare, very strong field localization reaching almost $W_a/W_0 = 25$ is observed. This means that these modes can efficiently

trap light within the nanoantenna due to the high coupling efficiency to the probe near-field.

The estimated $Q-$factors of the nanotriangle modes are generally lower than the maximum values observed for the nanosquare antenna and are compared to the nanodisk CMs. For $y-$polarized illumination, we obtained $Q-$factors of $Q = 21$ for TM_{42}^e, $Q = 19$ for TE_{21}^e, and $Q = 15$ for TM_{32}^e (Figure 3(e) and (g)). For $x-$polarized illumination we observed $Q-$factors of $Q = 24$ for TE_{32}^o and $Q = 19$ for TE_{21}^o (Figure 4(e)).

However, the SNOM probe–antenna interactions can modify the modal excitation boundary conditions as well as the absorption and scattering of the optical modes. To reveal the influence of the SNOM probe on the Q-factor and resonant wavelength, we compared these parameters calculated from the SNOM data (spectral dependence of electric field localization W_a/W_0) with eigenmode analysis without the SNOM probe. Tables S1–S3 in Supplementary Materials, Section 5 show results for optical modes in the nanodisk, nanosquare, and nanotriangle, respectively. For optical modes with Q > 40 (obtained from SNOM W_a/W_0 data), Q-factors obtained from eigenmode analysis are almost two times larger than the results from SNOM spectral data. In contrast, the eigenmode analysis has similar values for the low Q optical modes (Q < 30 obtained from the SNOM data analysis). The more significant difference of the Q-factors for high Q modes (Q > 40) can be associated with the influence of the SNOM probe on excited optical modes. The SNOM probe leads to the additional light scattering and absorption of the optical modes that decrease their Q-factor. Low Q modes already have multiple channels for radiative and absorption losses. Therefore, adding one more channel (an SNOM probe) will not substantially impact the new Q-factor. In contrast, the impact on a high Q mode will be more prominent. Tables S1–S3 also show that the SNOM probe has only a small impact on the resonant wavelengths. This can be explained by the localization of the optical modes inside the volume of the nanoantennas.

It should be noted that the excitation of the optical modes near nanoantennas' edges leads to higher electric field localization than at other probe positions. TE_{43}^{eo} excited near the edge of the nanosquare leads to $W_a/W_0 = 11$ (Figure 2(e), circle mark) in comparison to 4.3 and 4.7 at two other positions (diamond mark in Figure 2(g) and triangle mark in Figure 2(h)). Also, for the nanosquare, excitation of TE_{33}^{oo} near the square edge leads to almost $W_a/W_0 = 25$ (Figure 2(f)), which is considerably higher than $W_a/W_0 = 12$ obtained at the position near the square center (Figure 2(h)). The excitation of TE_{21}^e (Figure 3(g)),

TE_{32}^o (Figure 4(e)), and TE_{21}^o (Figure 4(h)) in the nanotriangle results in higher field localization (W_a/W_0 is around 3) at the triangle's corner and base than other excitation positions.

The variable coupling efficiency that is observed originates from differences in the field overlap of the optical modes and near-field around the SNOM probe. This overlap is strongly governed by the spatial distribution of the field antinodes. Depending on the mode spatial structures, the field antinodes can be closer or farther from each other. It also depends on the wavelength of the excitation. For the disk, square, and triangle nanoantennas, the spatial distribution of the excited optical modes is different, which modifies the overlap of the optical modes with the near-field of the SNOM probe. The coupling efficiency is also governed by their intrinsic losses. The ratio of the radiative and absorption loss of the optical modes determines the coupling efficiency [75, 76]. All incident light can be coupled with the optical antenna modes at the equivalence between these two quantities. In other cases, the SNOM probe near-field light is more efficiently absorbed or scattered. As each mode has its own radiative loss, different modes possess a different coupling efficiency with the SNOM probe near-field.

2.5 Plane wave excitation

The higher order CMs and WGMs studied above by the SNOM probe excitation are difficult to be observed by far-field techniques using a plane wave source. For comparison, in Section 6, Supplementary Materials, we applied a plane wave source with normal incidence to drive the optical modes in the nanoantenna. It is shown that for the nanodisk, nanosquare, and nanotriangle such an approach allows the coupling to only a limited number of modes. The inability to excite all antenna supported modes is associated with a symmetry mismatch of the electromagnetic fields of the modes and the plane wave source. Moreover, even for the symmetry-allowed modes studied above, low coupling efficiency with a normal-incidence plane wave source complicates their excitation and observation.

3 Conclusions

Aperture type scanning near-field optical microscopy (SNOM) reveals a very rich variety of near-field optical patterns in amorphous silicon nanoantennas. The subwavelength localized excitation of higher order optical cavity modes (CMs) and whispering gallery modes (WGMs)

strongly depends on the nanoantennas shape, probe position, and excitation frequency. This has been demonstrated for some of the most basic geometries with varying rotational symmetries: a disk, square, and triangle. A detailed analysis based on full-field FDTD simulations allowed us to link the aperture SNOM maps to the field distributions of higher order modes supported by the nanoantennas which have not been previously visualized. The experimental data has been reconstructed based on the decomposition in CMs and WGMs with different order and parity. The insights obtained within this study for basic antenna cavity shapes provide an important foundation for the detailed understanding of the optical behavior of more complex nanocavity systems under local excitation and the interpretation of experimental near-field data. The local excitation of CMs and WGMs with even and odd symmetry is accompanied by very distinct light scattering and trapping properties that have a direct impact on e.g. the quantum efficiency of nearby emitters, the efficiency of non-linear effects [77, 78], and directionality of scattered or emitted light [19, 79].

Author contribution: All the authors have accepted responsibility for the entire content of this submitted manuscript and approved submission.

Conflict of interest statement: The authors declare no conflicts of interest regarding this article.

References

[1] A. I. Kuznetsov, A. E. Miroshnichenko, M. L. Brongersma, Y. S. Kivshar, and B. Luk'yanchuk, "Optically resonant dielectric nanostructures," *Science*, vol. 354, p. aag2472, 2016.

[2] N. Yu and F. Capasso, "Flat optics with designer metasurfaces," *Nat. Mater.*, vol. 13, no. 2, pp. 139−150, 2014.

[3] D. Lin, P. Fan, E. Hasman, and M. L. Brongersma, "Dielectric gradient metasurface optical elements," *Science*, vol. 345, no. 6194, pp. 298−302, 2014.

[4] A. Arbabi, Y. Horie, M. Bagheri, and A. Faraon, "Dielectric metasurfaces for complete control of phase and polarization with subwavelength spatial resolution and high transmission," *Nat. Nanotechnol.*, vol. 10, no. 11, pp. 937−943, 2015.

[5] M. K. Kroychuk, A. S. Shorokhov, D. F. Yagudin, et al., "Enhanced nonlinear light generation in oligomers of silicon nanoparticles under vector beam illumination," *Nano Lett*, vol. 20, no. 5, pp. 3471−3477, 2020.

[6] K. I. Okhlopkov, P. A. Shafirin, A. A. Ezhov, N. A. Orlikovsky, M. R. Shcherbakov, and A. A. Fedyanin, "Optical coupling between resonant dielectric nanoparticles and dielectric nanowires probed by third harmonic generation microscopy," *ACS Photonics*, vol. 6, no. 1, pp. 189−195, 2019.

[7] F. J. F. Löchner, A. N. Fedotova, S. Liu, et al., "Polarization-dependent second harmonic diffraction from resonant GaAs metasurfaces," *ACS Photonics*, vol. 5, no. 5, pp. 1786−1793, 2018.

[8] M. K. Kroychuk, D. F. Yagudin, A. S. Shorokhov, et al., "Tailored nonlinear anisotropy in Mie-resonant dielectric oligomers," *Adv. Opt. Mater.*, vol. 7, no. 20, p. 1900447, 2019.

[9] V. V. Zubyuk, P. P. Vabishchevich, M. R. Shcherbakov, et al., "Low-power absorption saturation in semiconductor metasurfaces," *ACS Photonics*, vol. 6, no. 11, pp. 2797−2806, 2019.

[10] M. G. Barsukova, A. S. Shorokhov, A. I. Musorin, D. N. Neshev, Y. S. Kivshar, and A. A. Fedyanin, "Magneto-optical response enhanced by Mie resonances in nanoantennas," *ACS Photonics*, vol. 4, no. 10, pp. 2390−2395, 2017.

[11] A. M. Chernyak, M. G. Barsukova, A. S. Shorokhov, A. I. Musorin, and A. A. Fedyanin, "Bound states in the continuum in magnetophotonic metasurfaces," *JETP Lett.*, vol. 111, no. 1, pp. 46−49, 2020.

[12] M. R. Shcherbakov, P. P. Vabishchevich, A. S. Shorokhov, et al., "Ultrafast all-optical switching with magnetic resonances in nonlinear dielectric nanostructures," *Nano Lett.*, vol. 15, no. 10, pp. 6985−6990, 2015.

[13] M. R. Shcherbakov, S. Liu, V. V. Zubyuk, et al., "Ultrafast all-optical tuning of direct-gap semiconductor metasurfaces," *Nat. Commun.*, vol. 8, no. 1, p. 17, 2017.

[14] S. Liu, A. Vaskin, S. Addamane, et al., "Light-emitting metasurfaces: simultaneous control of spontaneous emission and far-field radiation," *Nano Lett.*, vol. 18, no. 11, pp. 6906−6914, 2018.

[15] A. Vaskin, S. Mashhadi, M. Steinert, et al., "Manipulation of magnetic dipole emission from Eu3+ with Mie-resonant dielectric metasurfaces," *Nano Lett.*, vol. 19, no. 2, pp. 1015−1022, 2019.

[16] D. A. Shilkin, M. R. Shcherbakov, E. V. Lyubin, et al., "Optical magnetism and fundamental modes of nanodiamonds," *ACS Photonics*, vol. 4, no. 5, pp. 1153−1158, 2017.

[17] I. Staude, A. E. Miroshnichenko, M. Decker, et al., "Tailoring directional scattering through magnetic and electric resonances in subwavelength silicon nanodisks," *ACS Nano*, vol. 7, no. 9, pp. 7824−7832, 2013.

[18] Y. H. Fu, A. I. Kuznetsov, A. E. Miroshnichenko, Y. F. Yu, and B. Luk'yanchuk, "Directional visible light scattering by silicon nanoparticles," *Nat. Commun.*, vol. 4, no. 1, p. 1527, 2013.

[19] J. Li, N. Verellen, D. Vercruysse, T. Bearda, L. Lagae, and P. Van Dorpe, "All-dielectric antenna wavelength router with bidirectional scattering of visible light," *Nano Lett.*, vol. 16, no. 7, pp. 4396−4403, 2016.

[20] D. N. Gulkin, A. A. Popkova, B. I. Afinogenov, et al., "Mie-driven directional nanocoupler for Bloch surface wave photonic platform," *Nanophotonics*, vol. 10, no. 11, pp. 2939−2947, 2021.

[21] A. B. Khanikaev and G. Shvets, "Two-dimensional topological photonics," *Nat. Photonics*, vol. 11, no. 12, pp. 763−773, 2017.

[22] S. Kruk, A. Slobozhanyuk, D. Denkova, et al., "Edge states and topological phase transitions in chains of dielectric nanoparticles," *Small*, vol. 13, no. 11, p. 1603190, 2017.

[23] A. E. Krasnok, A. E. Miroshnichenko, P. A. Belov, and Y. S. Kivshar, "All-dielectric optical nanoantennas," *Opt. Express*, vol. 20, no. 18, pp. 20599−20604, 2012.

[24] L. Cao, P. Fan, E. S. Barnard, A. M. Brown, and M. L. Brongersma, "Tuning the color of silicon nanostructures," *Nano Lett.*, vol. 10, no. 7, pp. 2649−2654, 2010.

[25] A. B. Evlyukhin, S. M. Novikov, U. Zywietz, et al., "Demonstration of magnetic dipole resonances of dielectric nanospheres in the visible region," *Nano Lett.*, vol. 12, no. 7, pp. 3749−3755, 2012.

[26] L. Huang, Y. Yu, and L. Cao, "General modal properties of optical resonances in subwavelength nonspherical dielectric structures," *Nano Lett.*, vol. 13, no. 8, pp. 3559−3565, 2013.

[27] A. I. Kuznetsov, A. E. Miroshnichenko, Y. H. Fu, J. Zhang, and B. Luk'yanchuk, "Magnetic light," *Sci. Rep.*, vol. 2, no. 1, p. 492, 2012.

[28] H.-S. Ee, J.-H. Kang, M. L. Brongersma, and M.-K. Seo, "Shape-dependent light scattering properties of subwavelength silicon nanoblocks," *Nano Lett.*, vol. 15, no. 3, pp. 1759−1765, 2015.

[29] N. Verellen, F. López-Tejeira, R. Paniagua-Domínguez, et al, "Mode parity-controlled Fano- and Lorentz-like line shapes arising in plasmonic nanorods," *Nano Lett.*, vol. 14, no. 5, pp. 2322−2329, 2014.

[30] D. J. Traviss, M. K. Schmidt, J. Aizpurua, and O. L. Muskens, "Antenna resonances in low aspect ratio semiconductor nanowires," *Opt. Express*, vol. 23, no. 17, pp. 22771−22787, 2015.

[31] G. Schider, J. R. Krenn, A. Hohenau, et al., "Plasmon dispersion relation of Au and Ag nanowires," *Phys. Rev. B*, vol. 68, no. 15, p. 155427, 2003.

[32] M. K. Krug, M. Reisecker, A. Hohenau, et al., "Probing plasmonic breathing modes optically," *Appl. Phys. Lett.*, vol. 105, no. 17, p. 171103, 2014.

[33] M. Liu, T.-W. Lee, S. K. Gray, P. Guyot-Sionnest, and M. Pelton, "Excitation of dark plasmons in metal nanoparticles by a localized emitter," *Phys. Rev. Lett.*, vol. 102, no. 10, p. 107401, 2009.

[34] T. H. Taminiau, F. D. Stefani, and N. F. van Hulst, "Optical nanorod antennas modeled as cavities for dipolar emitters: evolution of sub- and super-radiant modes," *Nano Lett.*, vol. 11, no. 3, pp. 1020−1024, 2011.

[35] M. Kajetan Schmidt, S. Mackowski, and J. Aizpurua, "Control of single emitter radiation by polarization- and position-dependent activation of dark antenna modes," *Opt. Lett.*, vol. 37, no. 6, pp. 1017−1019, 2012.

[36] Z. Gao, L. Yin, W. Fang, et al., "Imaging Chladni figure of plasmonic charge density wave in real space," *ACS Photonics*, vol. 6, no. 11, pp. 2685−2693, 2019.

[37] T. Coenen, J. van de Groep, and A. Polman, "Resonant modes of single silicon nanocavities excited by electron irradiation," *ACS Nano*, vol. 7, no. 2, pp. 1689−1698, 2013.

[38] J. van de Groep, T. Coenen, S. A. Mann, and A. Polman, "Direct imaging of hybridized eigenmodes in coupled silicon nanoparticles," *Optica*, vol. 3, no. 1, pp. 93−99, 2016.

[39] D. Rossouw, M. Couillard, J. Vickery, E. Kumacheva, and G. A. Botton, "Multipolar plasmonic resonances in silver nanowire antennas imaged with a subnanometer electron probe," *Nano Lett.*, vol. 11, no. 4, pp. 1499−1504, 2011.

[40] F.-P. Schmidt, H. Ditlbacher, U. Hohenester, A. Hohenau, F. Hofer, and J. R. Krenn, "Dark plasmonic breathing modes in silver nanodisks," *Nano Lett.*, vol. 12, no. 11, pp. 5780−5783, 2012.

[41] E. P. Bellido, A. Manjavacas, Y. Zhang, Y. Cao, P. Nordlander, and G. A. Botton, "Electron energy-loss spectroscopy of multipolar edge and cavity modes in silver nanosquares," *ACS Photonics*, vol. 3, no. 3, pp. 428−433, 2016.

[42] A. Campos, A. Arbouet, J. Martin, et al., "Plasmonic breathing and edge modes in aluminum nanotriangles," *ACS Photonics*, vol. 4, no. 5, pp. 1257−1263, 2017.

[43] M.-W. Chu, V. Myroshnychenko, C. H. Chen, J.-P. Deng, C.-Y. Mou, and F. J. García de Abajo, "Probing bright and dark surface-plasmon modes in individual and coupled noble metal nanoparticles using an electron beam," *Nano Lett.*, vol. 9, no. 1, pp. 399−404, 2009.

[44] A. L. Koh, A. I. Fernández-Domínguez, D. W. McComb, S. A. Maier, and J. K. W. Yang, "High-resolution mapping of electron-beam-excited plasmon modes in lithographically defined gold nanostructures," *Nano Lett.*, vol. 11, no. 3, pp. 1323−1330, 2011.

[45] T. Coenen, D. T. Schoen, S. A. Mann, et al., "Nanoscale spatial coherent control over the modal excitation of a coupled plasmonic resonator system," *Nano Lett.*, vol. 15, no. 11, pp. 7666−7670, 2015.

[46] J. Dorfmüller, R. Vogelgesang, R. T. Weitz, et al., "Fabry−Pérot resonances in one-dimensional plasmonic nanostructures," *Nano Lett.*, vol. 9, no. 6, pp. 2372−2377, 2009.

[47] S. Usui, S. Kitade, I. Morichika, K. Kohmura, F. Kusa, and S. Ashihara, "Near-field imaging of infrared nanoantenna modes under oblique illumination," *J. Phys. Chem. C*, vol. 121, no. 46, pp. 26000−26006, 2017.

[48] R. Esteban, R. Vogelgesang, J. Dorfmüller, et al., "Direct near-field optical imaging of higher order plasmonic resonances," *Nano Lett.*, vol. 8, no. 10, pp. 3155−3159, 2008.

[49] M. Rang, A. C. Jones, F. Zhou, et al., "Optical near-field mapping of plasmonic nanoprisms," *Nano Lett.*, vol. 8, no. 10, pp. 3357−3363, 2008.

[50] M. Schnell, A. García-Etxarri, A. J. Huber, K. Crozier, J. Aizpurua, and R. Hillenbrand, "Controlling the near-field oscillations of loaded plasmonic nanoantennas," *Nat. Photonics*, vol. 3, no. 5, pp. 287−291, 2009.

[51] J. Dorfmüller, D. Dregely, M. Esslinger, et al., "Near-field dynamics of optical Yagi-Uda nanoantennas," *Nano Lett.*, vol. 11, no. 7, pp. 2819−2824, 2011.

[52] T. G. Habteyes, I. Staude, K. E. Chong, et al., "Near-field mapping of optical modes on all-dielectric silicon nanodisks," *ACS Photonics*, vol. 1, no. 9, pp. 794−798, 2014.

[53] V. A. Zenin, A. B. Evlyukhin, S. M. Novikov, et al., "Direct amplitude-phase near-field observation of higher-order anapole states," *Nano Lett.*, vol. 17, no. 11, pp. 7152−7159, 2017.

[54] A. E. Miroshnichenko, A. B. Evlyukhin, Y. F. Yu, et al., "Nonradiating anapole modes in dielectric nanoparticles," *Nat. Commun.*, vol. 6, no. 1, p. 8069, 2015.

[55] R. M. Bakker, D. Permyakov, Y. F. Yu, et al., "Magnetic and electric hotspots with silicon nanodimers," *Nano Lett.*, vol. 15, no. 3, pp. 2137−2142, 2015.

[56] D. Denkova, N. Verellen, A. V. Silhanek, V. K. Valev, P. V. Dorpe, and V. V. Moshchalkov, "Mapping magnetic near-field distributions of plasmonic nanoantennas," *ACS Nano*, vol. 7, no. 4, pp. 3168−3176, 2013.

[57] T. Matsuura, K. Imaeda, S. Hasegawa, H. Suzuki, and K. Imura, "Characterization of overlapped plasmon modes in a gold hexagonal plate revealed by three-dimensional near-field optical microscopy," *J. Phys. Chem. Lett.*, vol. 10, no. 4, pp. 819−824, 2019.

[58] D. Denkova, N. Verellen, A. V. Silhanek, P. Van Dorpe, and V. V. Moshchalkov, "Lateral magnetic near-field imaging of plasmonic nanoantennas with increasing complexity," *Small*, vol. 10, no. 10, p. 1959−2021, 1966.

[59] H. Okamoto and K. Imura, "Visualizing the optical field structures in metal nanostructures," *J. Phys. Chem. Lett.*, vol. 4, no. 13, pp. 2230−2241, 2013.

[60] A. Y. Frolov, N. Verellen, J. Li, et al., "Near-field mapping of optical Fabry−Perot modes in all-dielectric nanoantennas," *Nano Lett.*, vol. 17, no. 12, pp. 7629−7637, 2017.

[61] E. F. F. Chladni, *Treatise on Acoustics*, Springer, 2015.

[62] D. Denkova, N. Verellen, A. V. Silhanek, P. Van Dorpe, and V. V. Moshchalkov, *Near-field aperture-probe as a magnetic dipole source and optical magnetic field detector*, 2014. arXiv:1406.7827v1.

[63] R. K. Mongia and P. Bhartia, "Dielectric resonator antennas—a review and general design relations for resonant frequency and bandwidth," *Int. J. Microw. Millim.-Wave Comput.-Aided Eng.*, vol. 4, no. 3, pp. 230−247, 1994.

[64] B. Hecht, B. Sick, U. P. Wild, et al., "Scanning near-field optical microscopy with aperture probes: fundamentals and applications," *J. Chem. Phys.*, vol. 112, no. 18, pp. 7761−7774, 2000.

[65] K. Imura, K. Ueno, H. Misawa, and H. Okamoto, "Anomalous light transmission from plasmonic-capped nanoapertures," *Nano Lett.*, vol. 11, no. 3, pp. 960−965, 2011.

[66] K. Imura, T. Nagahara, and H. Okamoto, "Characteristic near-field spectra of single gold nanoparticles," *Chem. Phys. Lett.*, vol. 400, no. 4, pp. 500−505, 2004.

[67] K. Imura, T. Nagahara, and H. Okamoto, "Near-field optical imaging of plasmon modes in gold nanorods," *J. Chem. Phys.*, vol. 122, no. 15, p. 154701, 2005.

[68] K. Imura, K. Ueno, H. Misawa, et al., "Plasmon modes in single gold nanodiscs," *Opt. Express*, vol. 22, no. 10, pp. 12189−12199, 2014.

[69] A. Y. Nikitin, P. Alonso-González, S. Vélez, et al., "Real-space mapping of tailored sheet and edge plasmons in graphene nanoresonators," *Nat. Photonics*, vol. 10, no. 4, pp. 239−243, 2016.

[70] G. M. Wysin, "Electromagnetic modes in dielectric equilateral triangle resonators," *J. Opt. Soc. Am. B*, vol. 23, no. 8, pp. 1586−1599, 2006.

[71] C. Wang, "Exact solution of equilateral triangular waveguide," *Electron. Lett.*, vol. 46, no. 13, pp. 925−927, 2010.

[72] A. Alex-Amor, G. Valerio, F. Ghasemifard, et al., "Wave propagation in periodic metallic structures with equilateral triangular holes," *Appl. Sci.*, vol. 10, no. 5, p. 1600, 2020.

[73] G. Wysin. https://www.phys.ksu.edu/personal/wysin/OpticalModes/tripics/index.html.

[74] D. G. Baranov, D. A. Zuev, S. I. Lepeshov, et al., "All-dielectric nanophotonics: the quest for better materials and fabrication techniques," *Optica*, vol. 4, no. 7, pp. 814−825, 2017.

[75] T. J. Seok, A. Jamshidi, M. Kim, et al., "Radiation engineering of optical antennas for maximum field enhancement," *Nano Lett.*, vol. 11, no. 7, pp. 2606−2610, 2011.

[76] M. L. Gorodetsky and V. S. Ilchenko, "Optical microsphere resonators: optimal coupling to high-Q whispering-gallery modes," *J. Opt. Soc. Am. B*, vol. 16, no. 1, pp. 147−154, 1999.

[77] N. Verellen, D. Denkova, B. D. Clercq, et al., "Two-photon luminescence of gold nanorods mediated by higher order plasmon modes," *ACS Photonics*, vol. 2, no. 3, pp. 410−416, 2015.

[78] T.-Y. Chen, J. Obermeier, T. Schumacher, et al., "Modal symmetry controlled second-harmonic generation by propagating plasmons," *Nano Lett.*, vol. 19, no. 9, p. 6424−6428, 2019.

[79] D. Vercruysse, X. Zheng, Y. Sonnefraud, et al., "Directional fluorescence emission by individual V-antennas explained by mode expansion," *ACS Nano*, vol. 8, no. 8, pp. 8232−8241, 2014.